RSC Advances

PAPER

View Article Online
View Journal | View Issue

Cite this: *RSC Adv.*, 2025, **15**, 37012

Engineering a GelMA–dECM-based 3D bioprinted liver fibrosis model: methotrexate-induced functional and molecular validation

Mrunmayi Gadre and Kirthanashri S. Vasanthan*

Received 13th August 2025
Accepted 29th September 2025

DOI: 10.1039/d5ra05955k

rsc.li/rsc-advances

Three-dimensional (3D) bioprinting represents a cutting-edge advancement in additive manufacturing, offering unprecedented precision in fabricating *in vitro* models that recapitulate native tissue architecture and function. Here, we present the fabrication of a bioprinted hepatic construct using a composite bioink composed of in-house synthesized gelatin methacryloyl (GelMA), rat liver-derived decellularized extracellular matrix (dECM), and HepG2 cells. GelMA imparted mechanical integrity and biocompatibility, while the liver-specific dECM provided bioactive cues critical for recapitulating the hepatic microenvironment. Constructs were crosslinked using microbial transglutaminase and a photoinitiator to ensure structural stability and shape fidelity. Functional characterization included cytocompatibility assays (MTT, live/dead), metabolic activity assays (albumin and urea secretion), and liver-specific enzyme analysis (LDH, ALT, and ALP), alongside gene expression profiling, all of which confirmed hepatic function within the constructs. This synergy enhances cellular functionality and supports accurate fibrosis modeling for translational research. To establish a fibrosis model, methotrexate (MTX) was introduced, resulting in functional decline and upregulation of fibrosis-associated genes, thereby validating the fibrotic phenotype. This study demonstrates the development of a robust and physiologically relevant 3D bioprinted *in vitro* platform for modeling MTX-induced liver fibrosis, providing a promising tool for preclinical drug screening and translational research in hepatic disease. This study demonstrates a robust and physiologically relevant 3D bioprinted *in vitro* model of methotrexate-induced liver fibrosis, offering a valuable platform for translational applications in drug screening and hepatic disease modelling.

1 Introduction

Three-dimensional (3D) bioprinting represents a sophisticated advancement in additive manufacturing, enabling precise fabrication of 3D constructs derived from computer-aided designs (CAD).[1,2] This technology necessitates the integration of viable cells and bioactive materials, known as bioinks, which facilitate the development of *in vitro* tissue models capable of mimicking the intricate physical and biochemical properties of native tissues. The core components of the bioprinting process include bioink formulation, selection of biomaterials, and advanced bioprinting techniques. The workflow involves three primary stages: pre-bioprinting, which includes creating a G-CODE based model and material selection; bioprinting, involving precise layer-by-layer deposition of bioinks; and post-bioprinting, focused on cellular maturation, proliferation, and functional validation of the fabricated constructs.[3–6]

The biomaterials selected for bioink formulations are typically chosen based on their capacity to support key cellular processes such as adhesion, proliferation, differentiation, and migration.[7–9] The selection of materials for the formation of bioink extends beyond simply supporting cellular processes such as adhesion, proliferation, differentiation, and migration. An ideal bioink demonstrates various properties including appropriate degradation kinetics, balancing stability with the need for eventual remodelling by cells.[10,11] Another equally important property is the mechanical stability that is required to provide structural support to the 3D scaffolds that are fabricated to mimic the native tissue viscoelasticity.[12] Shape fidelity and right printability viscosity are other aspects essential for accurate deposition of the bioink deposition and maintenance of 3D architecture post-printing,[13] in order for the 3D bioprinted structures to maintain their structure and prevent collapse. Thus, the design of liver-specific bioinks requires a fine balance between biological compatibility, mechanical integrity, printability, and long-term functionality.

Gelatin, a naturally derived polymer obtained through collagen denaturation, possesses intrinsic arginine–glycine–aspartic acid (RGD) motifs crucial for cellular attachment and communication. However, gelatin alone is biodegradable and mechanically unstable over extended periods.[14,15] To overcome

Manipal Centre for Biotherapeutic Research, Manipal Academy of Higher Education, Manipal-576104, Karnataka, India. E-mail: kirthanashri.sv@manipal.edu

these limitations, GelMA is synthesized by chemically modifying gelatin with methacrylic anhydride, resulting in enhanced mechanical stability and improved longevity. GelMA scaffolds exhibit suitable mechanical properties, excellent biocompatibility, and non-toxicity, and thus they are widely explored in diverse tissue engineering applications, including the culture of stem cells, hepatocytes, and cartilage regeneration.[16]

dECM obtained from native liver tissues, provides essential biochemical cues to replicate native organ-specific microenvironments. The decellularization process aims to effectively eliminate cellular components while preserving critical ECM components such as collagens, elastin, fibrillin, fibronectin, laminin, proteoglycans [including heparan sulphate, chondroitin sulfate, keratan sulfate, and glycosaminoglycans (GAGs)], and embedded growth factors.[17] Various decellularization strategies including physical, chemical, and enzymatic are employed, with rigorous evaluations performed to ensure effective removal of cellular remnants, thereby guaranteeing the cytocompatibility and structural integrity of the resulting dECM.[18–20] The established criteria for successful decellularization include dsDNA content of less than 50 ng per mg ECM dry weight,[21] DNA fragment lengths below 200 bp,[22] and the absence of visible nuclear materials verified through DAPI or Haematoxylin and Eosin (H&E) staining.[23] In this study, chemical decellularization *via* EDTA and sequential concentrations of sodium dodecyl sulfate (SDS) is utilized to produce liver-derived dECM.

Current *in vitro* liver fibrosis models often lack physiological complexity, functional robustness, and fail to adequately recapitulate the dynamic molecular events observed *in vivo*, limiting their translational applicability.[24] Most of the disease modelling systems include conventional 2D culture systems and simple hydrogel models, which are very simple and they fail to mimic the 3D architecture of native tissues. There is a lack of physical complexity such as the vascularized and mechanically dynamics.[25] There are limitations such as the cell–cell and cell–matrix interactions which play vital roles in maintaining hepatocyte phenotype and modelling fibrosis accurately. There is a lack of functional robustness such as long-term stability, with hepatocyte functions in other models. Thus, the availability of 3D bioprinted scaffolds that are specific to chronic toxicity or fibrosis studies are limited.[26] There is also an unavailability of model that can recapitulate the molecular events like the fibrosis, as the process is driven by complex molecular mechanisms.

The present study addresses these gaps by combining GelMA, providing mechanical stability,[27] and liver-derived dECM, supplying native biochemical signalling cues,[28,29] to engineer a bioink specifically tailored for hepatic tissue engineering. Incorporation of HepG2 cells within this bioink facilitates the generation of liver constructs with improved structural and functional fidelity, enabling precise modeling of non-fibrotic and fibrotic liver conditions.[30–32] This innovative model not only enhances the physiological relevance and predictive accuracy for studying hepatic fibrosis but also significantly advances translational applications, including drug screening, toxicity evaluations, and disease modeling, ultimately accelerating the discovery of effective therapeutic interventions.[33,34]

2 Materials and methods

2.1 Materials

Dulbecco's modified Eagle's medium (DMEM), high glucose w/ 4.5 g glucose per litre, L-glutamine and sodium bicarbonate w/o sodium pyruvate and Dulbecco's phosphate-buffered saline (DPBS) was procured from Himedia, India. Fetal bovine serum (FBS) was got from Gibco. Penicillin/streptomycin, trypsin, trizol and methotrexate were ordered from Sigma-Aldrich and albumin (BCG) [ab235628] Assay Kit from Abcam. Lactate Dehydrogenase (LDH) activity [E-BC-K046-M] assay kit and Urea (BUN) Calorimetric based assay (Urease method) [E-BC-K183-M] were purchased from Elab sciences. The alanine transaminase (ALT) [ab241035] and alkaline phosphatase (ALP) [ab83369] calorimetric kit-based assay from Abcam. Sodium dodecyl sulfate, phenol, chloroform, isoamyl alcohol, isopropanol and papain were purchased from Sisco Research Laboratories, India. Ethylenediamine tetra acetic acid and formaldehyde was bought from Qualigens, India. Glutaraldehyde was ordered from Sigma-Aldrich, India. Proteinase K was purchased from Invitrogen, India. Coomassie brilliant blue and protease inhibitor cocktail was obtained from Merck, India. Sodium acetate was purchased from Tokyo Chemical Industry, India. RIPA buffer was procured from Himedia, India. Pierce™ CA Protein Assay Kit was purchased from Thermo Fisher Scientific, India and Blyscan™ – sulfated glycosaminoglycan (sGAG) assay kit from biocolor, United Kingdom, PrimeScript™ 1st strand cDNA Synthesis Kit and TB Green Premix Ex Taq (Tli RNase H Plus) was brought from Takara, USA.

2.2 Animal ethics approval

All the animals used in this study were approved by the Institutional Animal Ethics Committee (IAEC), Manipal Academy of Higher Education, Manipal which is in accordance with CPSCEA guidelines (IAEC/KMC/121/2022). All the experiments involving the animals were performed following ARRIVE guidelines.

2.3 Methods

2.3.1 Cell culture. Human hepatocellular carcinoma (HepG2) cells were procured from the National Centre for Cell Science (NCCS), Pune, India. Cells were cultured in Dulbecco's Modified Eagle Medium (DMEM) supplemented with 10% (v/v) fetal bovine serum (FBS) and 1% (v/v) penicillin–streptomycin (P/S). Cultures were maintained at 37 °C in a humidified atmosphere with 5% CO_2. Cells were routinely sub-cultured upon reaching 80–90% confluence using standard trypsinization protocols.

2.3.2 Liver harvest and decellularization protocol. Male Wistar rats (150–250 g; 9–12 weeks old) were anesthetized *via* intraperitoneal injection of sodium pentobarbital (50 mg kg^{-1}). Papaverine (20 mg kg^{-1}) was injected into the tail vein to relax the visceral muscles and to euthanize the animal. A transverse incision across the abdomen was made, and ligaments connecting to the liver lobes were carefully cut to expose liver. The liver was excised from the body and placed in a falcon tube with sterile phosphate buffer saline (PBS). The tissues were washed with sterile PBS and stored at 80 °C until further use.

The excised liver was rinsed with sterile distilled water and immersed in 0.001 M ethylenediaminetetraacetic acid (EDTA) for 30 minutes to facilitate initial matrix loosening. Post-treatment, the liver was sectioned into small fragments and perfused with 60 mL of distilled water to remove blood residues.

Decellularization was carried out following an optimized protocol previously reported by authors.[35] Briefly decellularization was carried through sequential perfusion with sodium dodecyl sulfate (SDS) at increasing concentrations (0.1%, 0.25%, 0.5%, 0.75%, and 1%, 60 mL each per concentration), introduced through 8–10 injection sites per tissue fragment to ensure uniform exposure. Upon completion, the tissue was rinsed extensively with distilled water until a translucent appearance was observed, indicating successful decellularization. The resulting decellularized extracellular matrix (dECM) was subjected to morphological and biochemical characterization, including DNA quantification, histological staining, protein profiling, and ultrastructural imaging *via* scanning electron microscopy (SEM).

2.3.3 Histological evaluation. Native and decellularized liver tissues were fixed in 10% neutral-buffered formalin and stored at ambient temperature until further processed by microtome method.[36] The 3D bioprinted scaffold were covered with optimal cutting temperature cryogel (Sakura Finetek, USA) and cryosectioning was performed in Cryostat RWD Minux FS800 (Crystal bio equipment). All the sections were stained in house, briefly the sections were washed with distilled water for 60 seconds, and the slides were dipped in haematoxylin for 10 minutes and washed under tap water for 5 minutes. Further the slides were subjected to eosin for 20 seconds and washed with 75% ethanol, followed by 90% and 100%. Once the slides were dried completely, they were fixed with Dibutylphthalate Polystyrene Xylene (DPX). Stained sections were visualized using an Olympus CX43 microscope (Olympus, Japan), and images were captured for histopathological comparison.

2.3.4 Scanning electron microscopy. To assess ultrastructural preservation, tissue samples were fixed in 2.5% glutaraldehyde at 4 °C for 2 hours. The fixed samples were dehydrated through a graded ethanol series (10–100%) with 10-minute intervals per step, followed by overnight drying at 37 °C.[37] SEM imaging was conducted using the ZEISS EVO MA18 scanning electron microscope (Carl Zeiss, Germany) at the Central Instrumentation Facility, Manipal Institute of Technology, MAHE.

2.3.5 Genomic DNA isolation and quantification. Genomic DNA was isolated from 50 mg of native and decellularized liver tissues using a phenol : chloroform : isoamyl alcohol extraction method ($n = 3$). Tissue homogenization was performed in 1× PBS using a Scilogex SCI16 PRO homogenizer (USA), followed by centrifugation at 5000 rpm for 10 minutes. The supernatant was discarded, and the pellet was treated with 200 µL of lysis buffer, 400 µL of phenol, and 10 µL of proteinase K. After mixing *via* Rotospin (25 rpm, 10 minutes), samples were incubated at 55 °C for 2 hours in a water bath.

Subsequent phase separation was performed using sequential extractions with phenol and a 1 : 1 mixture of chloroform : isoamyl alcohol (CIA), followed by centrifugation at 8000 rpm for 10 minutes after each extraction. The aqueous layer was collected and treated with chilled isopropanol and sodium acetate to precipitate DNA. The pellet was washed twice with 100% ethanol and dissolved in 1× TE buffer after air drying. The purity and yield of DNA were confirmed *via* 1% agarose gel electrophoresis and spectrophotometric analysis.

2.3.6 Quantification of total protein and glycosaminoglycans. Total protein content was quantified using the bicinchoninic acid (BCA) assay. Proteins were extracted from 50 mg of both native and decellularized tissues using 1× radioimmunoprecipitation assay (RIPA) buffer supplemented with protease inhibitor cocktail. Equal volumes of the lysate and working reagent from the BCA kit were mixed and incubated at 37 °C for 30 minutes. Absorbance was measured at 562 nm, and concentrations were interpolated from a standard curve.

The extracted protein samples were further resolved by sodium dodecyl sulfate-polyacrylamide gel electrophoresis (SDS-PAGE) using a 6% resolving and 4% stacking gel under constant voltage (100 V for 90 minutes). Gels were stained with Coomassie Brilliant Blue and imaged using the Invitrogen iBright CL1500 imaging system (Thermo Fisher Scientific).

2.3.7 Gelatin methacryloyl synthesis. GelMA was synthesized following an optimized protocol previously reported.[38] Briefly, gelatin type A (porcine, Bloom strength 175 g) was dissolved at a concentration of 10% (w/v) in phosphate-buffered saline (PBS, pH 7.4) at 50 °C. Methacrylic anhydride (MA) was added (0.6 g MA per 1 g gelatin) under vigorous stirring (1200 rpm) at 50 °C for 1 hour. The resultant mixture was centrifuged at 4000 rpm for 2 minutes to remove excess MA. The insoluble pellet was removed, and the supernatant was diluted with an equal volume of PBS. The diluted solution was then subjected to purification by dialysis against deionized water using a 10 kDa molecular weight cut-off (MWCO) dialysis membrane (Hi-Media, India). Dialysis was performed at 40 °C for 5 consecutive days, with the external deionized water replaced every 24 hours to ensure efficient removal of unreacted methacrylic anhydride, salts, and other low-molecular-weight impurities. The purified GelMA solution was lyophilized and stored at −20 °C until use. GelMA was characterized in comparison to native gelatin using Fourier-transform infrared spectroscopy (FTIR), which confirmed methacrylation through the detection of characteristic amide bond modifications.

2.3.8 Decellularized ECM solubilization. Decellularized liver tissue comprises extracellular matrix proteins such as collagen, elastin, fibrillin, fibronectin, laminin, proteoglycans (heparan sulfate, chondroitin sulfate, keratan sulfate, glycosaminoglycans), and embedded growth factors. Prior to incorporation into bioink formulations, dECM was solubilized by lyophilization for 72 hours, followed by milling into fine powder. The powder (2 mg mL^{-1}) was enzymatically digested with pepsin (10% w/w) in 0.5 N acetic acid at room temperature under constant stirring for 48 hours. Post-digestion, the solution was centrifuged (3000 rpm, 15 min), neutralized with 10 N sodium hydroxide, and quantified using BCA assay (Invitrogen). Protein integrity in solubilized dECM compared to native tissue was assessed by SDS-PAGE.

2.3.9 Computer-aided design (CAD) for bioprinting. CAD models for bioprinting were generated using OpenSCAD software and converted into stereolithography (STL) files. Model specifications, including dimensions and extrusion parameters, were defined precisely within the software. Bioprinting requires digital models typically obtained from imaging modalities (X-ray, computed tomography [CT], magnetic resonance imaging [MRI]) or designed directly through CAD software. All generated STL files underwent validation using computer-aided manufacturing (CAM) software prior to printing, ensuring compatibility and printability.[39–42] Bioink extrusion volumes were accurately calculated based on layer dimensions specified in STL files which were three layers in total.

2.3.10 Cytotoxicity analysis of solubilized dECM and GelMA on HepG2 cells. To evaluate potential cytotoxic effects of bioink components, solubilized dECM was added to HepG2 cell cultures at varying densities (10 μL dECM per 100 μL culture medium). Cell viability was assessed at 72 hours using the MTT assay. After incubation, media was removed, cells were briefly washed with PBS, and 100 μL of 0.5% MTT solution was added per well, incubated for 2 hours in darkness at 37 °C, followed by removal of MTT solution. Formazan crystals were dissolved by adding 100 μL DMSO per well, and absorbance readings were recorded at 570, 590, and 630 nm.

2.3.11 Characterization of 3D bioprinted constructs. GelMA-based bioink was formulated by combining lyophilized GelMA with lithium phenyl-2,4,6-trimethyl-benzoylphosphinate (LAP; Sigma-Aldrich, China), PBS, microbial transglutaminase (MTgase), solubilized rat liver dECM and HepG2 cells. Bioink was loaded into sterile syringes and extruded through a dual-extrusion bioprinter (Alfatek Systems, India) fitted with a 0.7 mm diameter needle at pressures of 120–180 kPa and deposition speed of 600 mm min^{-1} at room temperature. Constructs (1 × 1 cm) were printed in a rectilinear grid pattern and crosslinked using UV illumination in the presence of LAP. The 3D bioprinted scaffolds were observed under SEM and was found to have pore size of 90–120 μm.

2.3.11.1 Degradation study. Scaffold degradation was monitored by measuring initial wet weights, intermediate wet weights, and post-lyophilization dry weights at defined intervals. Structural changes and patterns on constructs were recorded using microscopy throughout the incubation period.

2.3.11.2 Induction of fibrosis. Fibrotic conditions were induced in HepG2 cells cultured on bioprinted constructs by exposure to 10 mM methotrexate, optimized from previous studies, over a 72-hour period. Post-treatment, cell viability was analyzed by MTT assay, and morphological evidence of fibrosis was evaluated using H&E staining. Cells were fixed in formaldehyde, sequentially dehydrated using graded ethanol washes, stained, and mounted with DPX prior to microscopic examination.

2.3.11.3 Live/dead viability assay. To corroborate MTT findings, viability of HepG2 cells post-fibrosis induction was assessed *via* live/dead fluorescent staining. After removing culture media and washing with Dulbecco's phosphate-buffered saline (DPBS), cells were incubated with a fresh live/dead reagent mixture (100 μL for 96-well plates or 200 μL for 24-well plates) in the dark at room temperature for 45 minutes. Fluorescent imaging was performed, and three-dimensional cell distributions were acquired using confocal Z-stack microscopy.

2.3.12 Biochemical assays. The biochemical markers including albumin, urea, lactate dehydrogenase (LDH), alkaline phosphatase (ALP), and alanine aminotransferase (ALT) were quantified from conditioned culture media using respective colorimetric assay kits, following the manufacturers' protocols. These markers were chosen based on their relevance to liver-specific functionality.

2.3.12.1 Albumin assay. Albumin levels were determined using a colorimetric assay kit based on the interaction of bromocresol green (BCG) with albumin, forming a chromophore measurable at 620 nm. In brief, 50 μL of culture supernatant was mixed with 100 μL of the reagent mix and incubated at room temperature for 25 minutes. The absorbance was measured at 620 nm using a microplate reader, and albumin concentration was quantified using a standard calibration curve.

2.3.12.2 Urea assay. Urea concentration was measured using a urease-based colorimetric kit, which catalyses the hydrolysis of urea to ammonia and carbon dioxide. The released ammonia reacts with a chromogenic reagent to produce a green-coloured complex detectable at 580 nm. A 4 μL sample aliquot was mixed with 50 μL of enzyme reagent and incubated at 37 °C for 10 minutes. Subsequently, 125 μL each of reagents 4 and 5 were added, followed by a second 10-minute incubation. Absorbance was measured at 580 nm, and urea concentrations were calculated from a standard curve.

2.3.12.3 Alkaline phosphatase (ALP) assay. ALP activity was evaluated using a high-throughput-compatible kit (Abcam) based on the hydrolysis of *p*-nitrophenyl phosphate (pNPP) to *p*-nitrophenol (pNP), detectable at 405 nm. Briefly, 50 μL of 5 mM pNPP was added to each well containing sample, followed by 10 μL of ALP enzyme solution in the standard wells. The reaction was incubated at 25 °C for 60 minutes, stopped using 20 μL of stop solution, and the absorbance was measured at 405 nm. The ALP concentration was extrapolated from a standard curve.

2.3.12.4 Alanine aminotransferase assay. ALT activity was assessed using a colorimetric ALT activity assay kit (Abcam). In brief, 0.5–2.5 μL of sample was adjusted to 5 μL with assay buffer. A freshly prepared 25 μL reaction mix was added to each well containing samples, standards, and controls. An additional 25 μL of background mix was added to background control wells. After incubation, the absorbance was read at 570 nm, and the ALT activity was calculated using a standard curve.

2.3.12.5 Lactate dehydrogenase assay. LDH activity was measured using a colorimetric kit based on the enzymatic conversion of lactic acid to pyruvic acid in the presence of coenzyme I. The resulting pyruvate forms a brownish-red hydrazone derivative with dinitrophenylhydrazine under alkaline conditions, detectable at 450 nm. Briefly, 200 μL of sample was mixed with 250 μL of substrate buffer and 50 μL of coenzyme I, followed by incubation at 37 °C for 15 minutes. Then, 250 μL of chromogenic agent was added and incubated again for 10 minutes. Finally, 2500 μL of alkaline developer was added, and absorbance was recorded at 450 nm. LDH concentration was calculated using a standard curve.

2.3.13 Gene expression analysis

2.3.13.1 RNA isolation. Scaffold samples were enzymatically digested using 1 mL of collagenase type I at 37 °C for 15–20 minutes. The digested material was centrifuged at 10 000 rpm for 5 minutes at 4 °C, washed with 1× PBS, and centrifuged again. The pellet was treated with 800 μL of TRIzol reagent followed by 160 μL of chloroform, vortexed, and incubated at room temperature for 2 minutes. After centrifugation at 12 000 rpm for 20 minutes at 4 °C, the upper aqueous phase was transferred to fresh tubes, and an equal volume of molecular-grade isopropanol was added. Following incubation and centrifugation at 13 000 rpm for 20 minutes, the RNA pellet was washed twice with ice-cold 70% ethanol and centrifuged at 7500 rpm for 5 minutes. The pellet was air-dried and resuspended in 10 μL of DEPC-treated water. RNA quantity was assessed using a microplate reader, and samples were stored at −80 °C.

2.3.13.2 cDNA synthesis. cDNA synthesis was performed using a commercial reverse transcription kit. The master mix was prepared as per the manufacturer's protocol, and 7 μL of the mix was aliquoted into sterile tubes along with the required volumes of RNA and dilution buffer. The thermal cycling conditions were 37 °C for 30 minutes, 85 °C for 5 seconds, and hold at 4 °C. Synthesized cDNA was stored at −20 °C.

2.3.13.3 Quantitative real-time PCR. qRT-PCR was carried out using a commercial SYBR green-based kit. Primer and template master mixes were prepared according to kit instructions. Each reaction contained 6 μL of primer mix and 4 μL of template mix. For the non-template control (NTC), 4 μL of DEPC water was added instead of the template. The thermal cycling conditions were:

- 95 °C for 30 seconds (initial denaturation).
- 40 cycles of 95 °C for 5 seconds and 60 °C for 34 seconds (amplification).
- Melting curve analysis: 95 °C for 15 seconds, 60 °C for 1 minute, and 95 °C for 15 seconds.

Post-run, reactions were stored at −20 °C for downstream analysis. Primer sequences are provided in the Table 1.

3 Results and discussion

3.1 Liver harvesting and decellularization outcomes

The decellularization of rat liver tissue was successfully accomplished within approximately 12 hours utilizing a stepwise chemical approach. Three freshly harvested rat livers were dissected into uniformly and sequentially exposed to EDTA, followed by graded concentrations of SDS (0.1%, 0.25%, 0.5%, 0.75%, and 1%). This controlled treatment effectively facilitated the removal of cellular components, as confirmed by visual assessment (Fig. 1). The native liver tissue initially exhibited a dark red appearance (Fig. 1A), progressively transitioning to a translucent state indicative of successful cell removal upon completion of the SDS treatment series (Fig. 1G).

Post-decellularization, liver matrices were stored at −80 °C in PBS containing sodium azide until subsequent analyses. Comparative analysis revealed a significant reduction in liver mass from pre-treatment to post-decellularization, resulting in dECM weight of approximately 1.1 g. Quantitatively, the average mass reduction from native liver tissue was approximately 87 ± 0.003%. Although weight reduction alone is insufficient to conclusively demonstrate complete decellularization, the consistent and substantial reduction observed aligns with effective cellular removal (Table 2). These findings were further substantiated through comprehensive biochemical and ultrastructural characterization studies.

3.2 Histological analysis

H&E staining was performed to evaluate the efficacy of decellularization and the preservation of the ECM structure. Microscopic examination revealed complete removal of cellular components from the dECM, as demonstrated by the absence of haematoxylin-positive nuclear staining (Fig. 2B). The dECM predominantly displayed eosin-positive staining (pink), indicative of retained ECM components such as collagen fibres. In contrast, the native liver tissue exhibited intense haematoxylin staining (purple), confirming the presence of intact nuclei and cellular structures along with ECM components (Fig. 2A). These histological findings substantiate successful decellularization, while maintaining the integrity of the liver ECM architecture.

3.3 Scanning electron microscopy analysis

SEM analysis was conducted to examine the ultrastructural alterations in liver tissue before and after decellularization.

Table 1 The forward and reverse primer sequences

Sr. no.	Primer name	Forward	Reverse
1	GAPDH	ACAGTCAGCCGCATCTTCTT	GACAAGCTTCCCGTTCTCAG
2	Albumin	GTCACCCACAATGTCCCCAT	CTCTGTCCACCTTCCAGCAG
3	Collagen I	GCCTGGTCAGAGAGGAGAGA	CTCCTGGTGAACAAGGTCCC
4	Cytochrome 3A4	GTCTTTGGGGCCTACAGCAT	CAATAAGGCACCACCCACCT
5	Cytochrome 2C9	TGTGGTCCTTGTGCTCTGTC	CCACTTTCATCCTGGGCTGT
6	Cytochrome 2E1	TTCTTTGCGGGGACAGAGAC	GGGTCAACGAGAGGCTTCAA
7	A-SMA	GTCACCCACAATGTCCCCAT	CTCTGTCCACCTTCCAGCAG
8	TIMP 1	CTCGTCATCAGGGCCAAGTT	CGGGCAGGATTCAGGCTATC

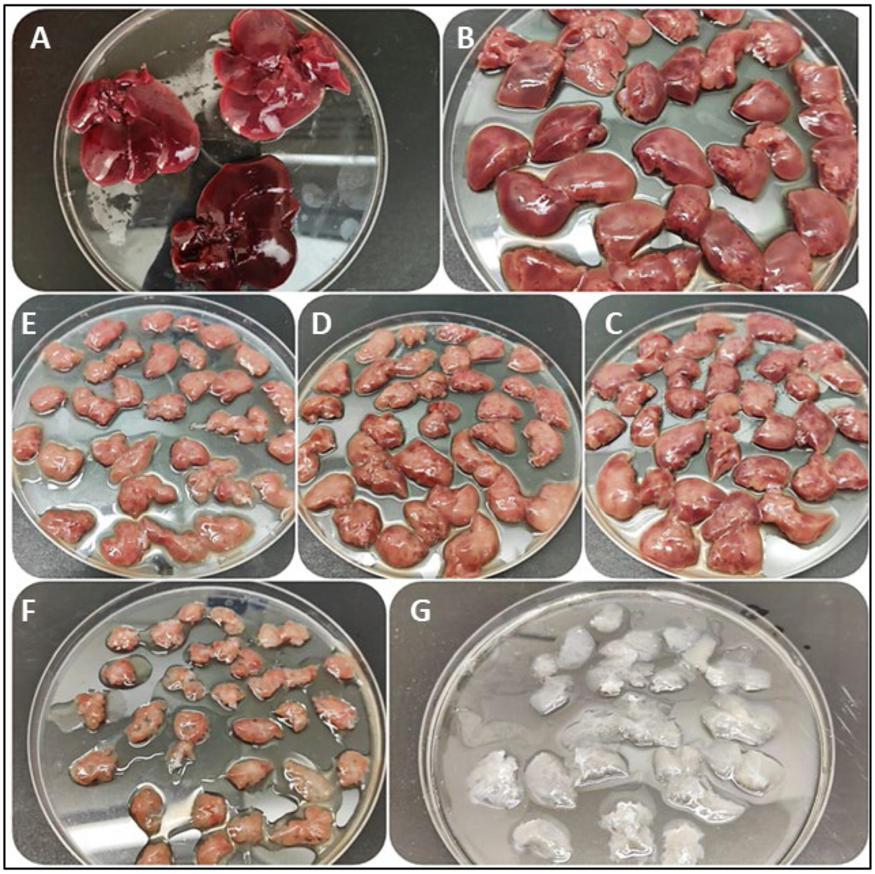

Fig. 1 Rat liver decellularization (A) – native liver; (B) – EDTA; (C to G) – gradually increasing concentrations of SDS (0.1%, 0.25%, 0.5%, 0.75% and 1%).

Table 2 Rat liver weight pre and post decellularization

Sr. no.	Weight of liver pre decellularization	Weight of liver post decellularization	Weight reduction %
1	9.1987	1.1569	87.42%
2	7.7963	0.9432	87.90%
3	8.8313	1.0608	87.98%

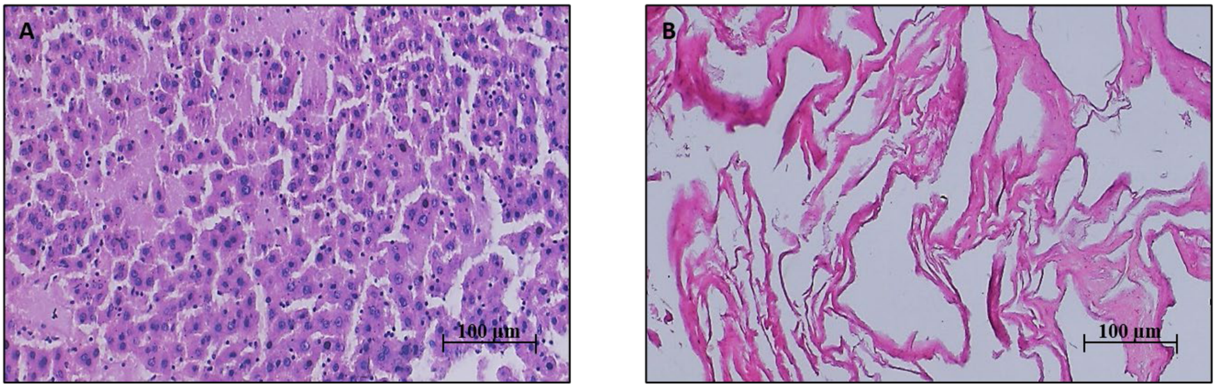

Fig. 2 H&E staining of (A) native liver tissue; (B) decellularized liver tissue (40× magnification).

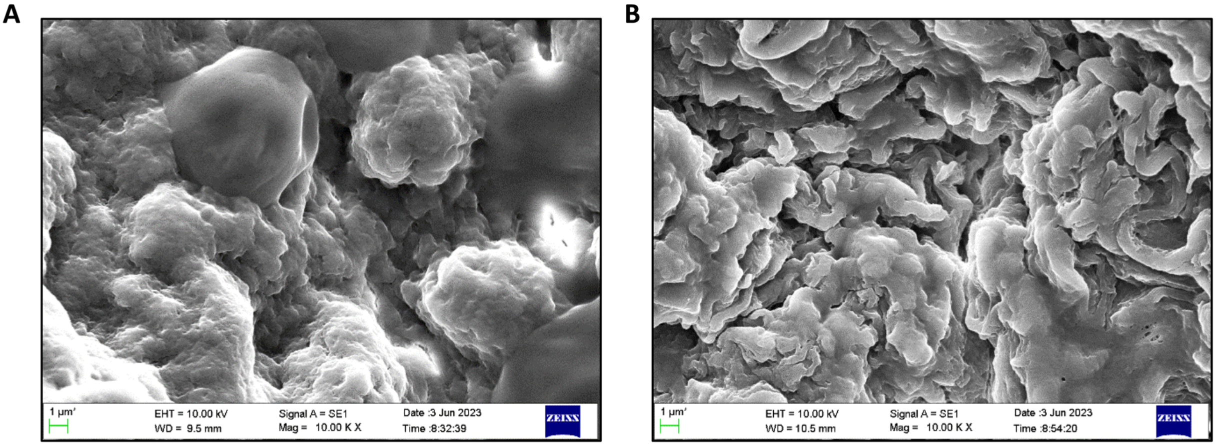

Fig. 3 SEM images of (A) native liver tissue; (B) decellularized liver tissue.

Representative SEM micrographs illustrated substantial differences between native liver tissue and dECM, as depicted in Fig. 3. Native liver tissue (Fig. 3A) displayed a densely packed architecture characterized by smooth, spherical cellular structures, indicative of intact hepatocytes. Conversely, the decellularized liver scaffold (Fig. 3B) exhibited a highly porous, fibrous ECM network devoid of cellular morphology, demonstrating successful cellular removal. These SEM findings confirm effective decellularization while preserving the essential ultrastructural integrity of the ECM, supporting its potential application as a scaffold for tissue engineering purposes.

3.4 DNA quantification and agarose gel electrophoresis

Quantitative and qualitative DNA assessments were conducted to confirm the effective removal of cellular components following decellularization. DNA content, normalized against the initial wet weight of each sample, demonstrated a significant reduction in the decellularized dECM compared to native liver tissue (Fig. 4A). Specifically, the DNA content in native liver was quantified as 1200 ± 8.05 ng mg^{-1}, while the dECM exhibited substantially reduced residual DNA at 10 ± 2.54 ng mg^{-1} (values expressed as mean ± SD, $n = 4$ per group).

Further confirmation through agarose gel electrophoresis (Fig. 4B) revealed prominent DNA bands in native liver samples, indicative of intact genomic material. In contrast, the absence of visible DNA bands in the dECM samples confirmed efficient genomic material removal, aligning with established standards for decellularization efficacy.

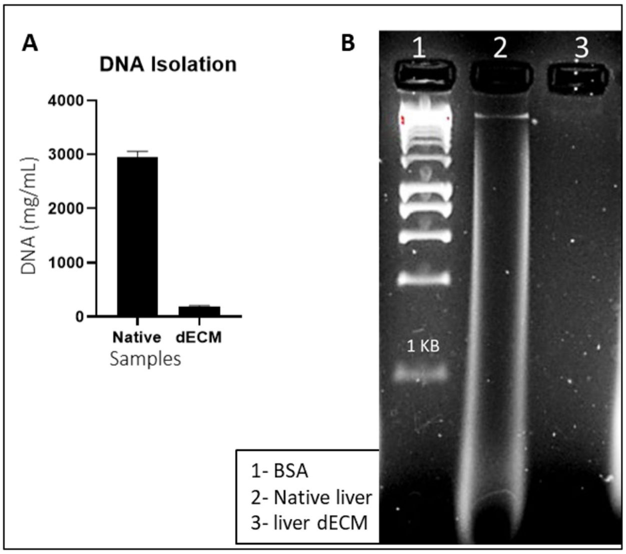

Fig. 4 (A) DNA concentration post isolation from native and dECM; *: statistically significant ($p < 0.0001$) (B) 1% agarose gel.

3.5 Total protein quantification and SDS-PAGE analysis

Protein integrity and composition in native liver, dECM, gelatin, and GelMA were evaluated through SDS-PAGE analysis and BCA quantification assay (Fig. 5). SDS-PAGE revealed distinct bands indicating the preservation of key extracellular matrix proteins, including the characteristic α1 and α2 chains of type I collagen at approximately 120 kDa and the β-chain at approximately 250 kDa (Fig. 5B). Comparative analysis confirmed similar protein profiles between native liver and dECM samples, demonstrating effective retention of ECM proteins post-decellularization. Quantitatively, total protein concentrations measured *via* BCA assay were as follows: gelatin, 1.20 ± 0.98 µg mL^{-1}; GelMA, 1.57 ± 1.20 µg mL^{-1}; native liver, 1.45 ± 0.67 µg mL^{-1}; and dECM, 1.28 ± 0.83 µg mL^{-1} (Fig. 5A). Results are presented as mean ± SD ($n = 4$ per group), suggesting minimal protein loss during the decellularization process.

3.6 Quantification of glycosaminoglycans (GAGs)

The sGAG content in native and decellularized rat liver tissues was quantified to assess ECM preservation post-decellularization. Fig. 6 demonstrates a moderate retention of sGAGs in dECM compared to native tissue, with concentrations quantified at 12.56 ± 1.20 µg mL^{-1} and 14.98 ± 0.95 µg mL^{-1}, respectively (mean ± SD; $n = 4$ per group). This significant retention of sGAG indicates that the decellularization protocol

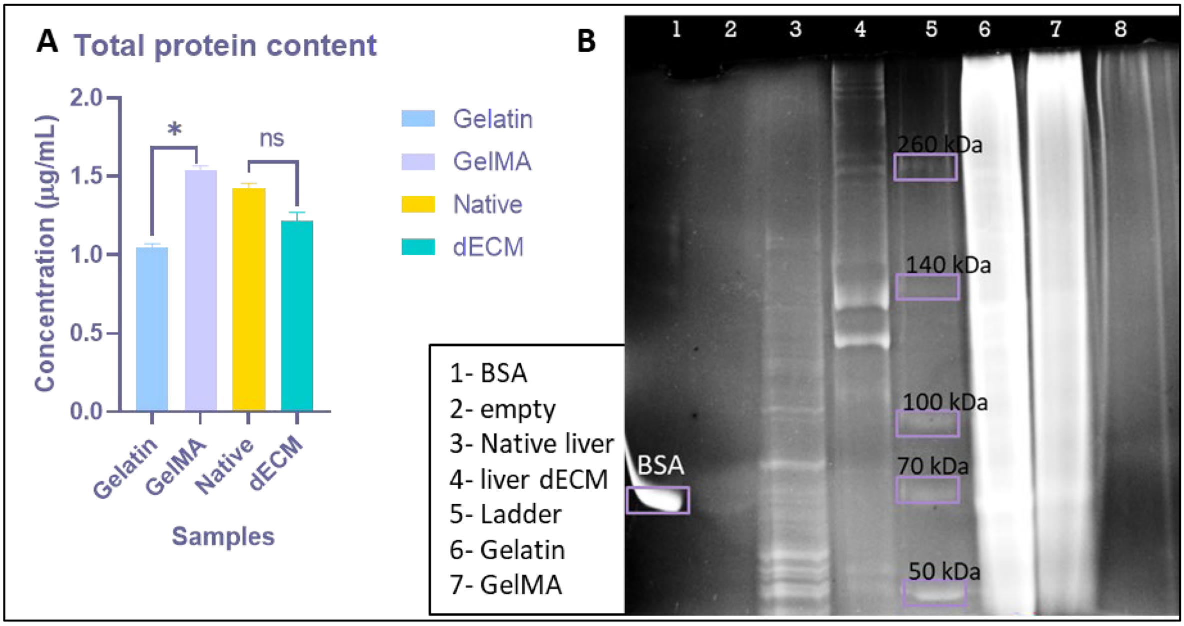

Fig. 5 Protein concentration post isolation from native and dECM (A) protein concentration *: statistically significant ($p < 0.05$) and ns: non-significant; (B) SDS PAGE of isolated proteins.

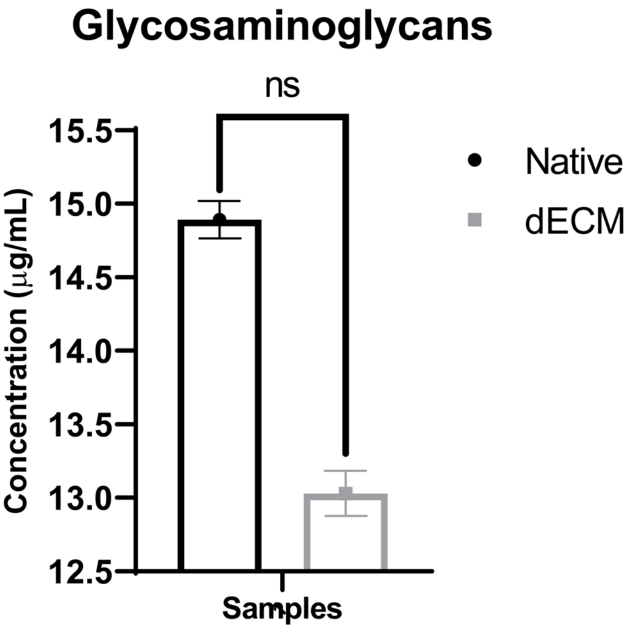

Fig. 6 sGAG concentration post isolation from native and dECM; ($p <$ 0.05) ns: non-significant.

preserved important ECM components, thereby enhancing the potential biological functionality of the dECM scaffold.

3.7 Gelatin methacryloyl synthesis

GelMA was synthesized and the characterization was performed using the FTIR and the presence of amide bonds were at different peaks. The peak at 1650 cm^{-1}, 1550 cm^{-1} and 1450 cm^{-1} confirmed the presence of amide bond I, II and III respectively (Fig. 7). The NMR was also performed and the degree of substitution was calculate to be 70% which was found sufficient for stability of GelMA. The other characterization of GelMA has already been studied and established in the patent filled by the research team.

3.8 Decellularized ECM solubilization

The SDS-PAGE was performed to determine the retention of the protein components in the solubilized dECM when compared with the extracted proteins from the native and dECM. Fig. 8B demonstrates the SDS-PAGE results and the presence of bands in all the days of solubilization when compared to both native and dECM. The bands were found in varying sizes confirming the presence of all types of proteins mainly, type I collagen at around 120 kDa and 250 kDa. The total protein content was quantified by BCA assay and was found to be 1.28 ± 0.18 µg mL^{-1} for day 1, 1.39 ± 0.12 µg mL^{-1} for day 2, 1.12 ± 0.11 µg mL^{-1} for day 3, 1.19 ± 0.09 µg mL^{-1} for day 4, 1.4 ± 0.14 µg mL^{-1} for native and 1.3 ± 0.19 µg mL^{-1} for dECM (Fig. 8A). The values are expressed as mean ± SD, with sample size of 04 on each day.

3.9 Computer-aided design for bioprinting

CAD models are digital designing through which the G-CODE to bioprint 3D models are generated (Fig. 9A). The grid pattern shown corresponds to the infill or filament pathway, critical for determining the porosity and internal structure of the printed scaffold (Fig. 9B). Actual photographic images of 3D-printed constructs (1 × 1 × 0.3 cm^3) (Fig. 9C). Close-up images show stacked, porous, lattice-like structures next to a ruler.

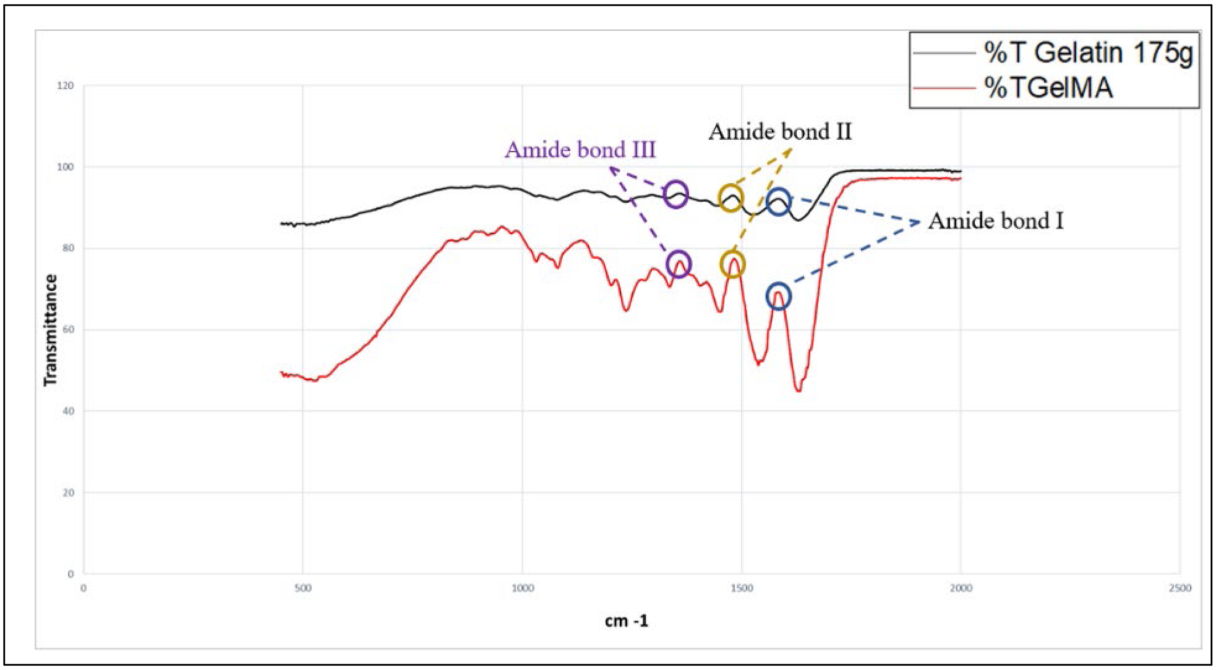

Fig. 7 FTIR graph of gelatin and GelMA.

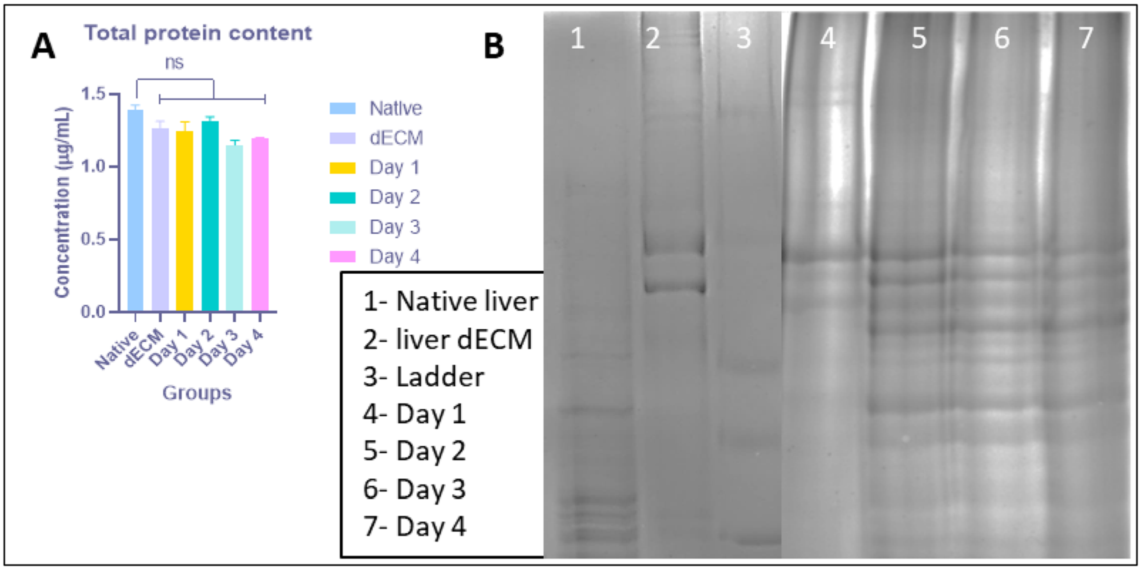

Fig. 8 (A) Total protein concentration post solubilization on different days, (B) SDS-PAGE of solubilized dECM; ($p < 0.05$) ns: non-significant.

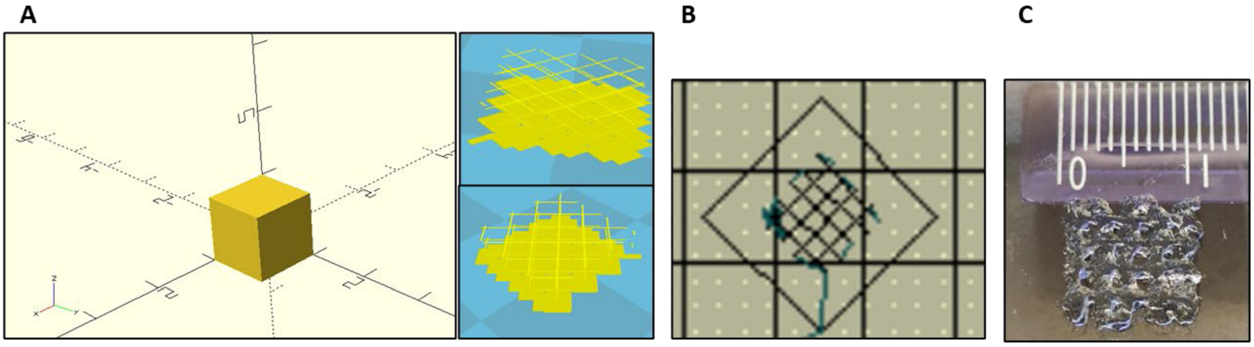

Fig. 9 3D designing (A) CAD models designed, (B) G-CODE generated, and (C) 3D printed with GelMA.

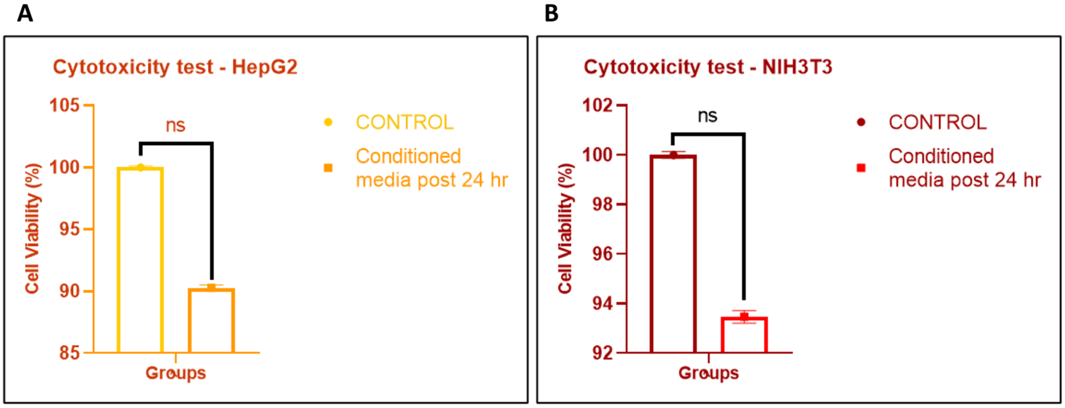

Fig. 10 Cytotoxicity of ink on (A) HepG2 cells and (B) NIH3T3 cells; (p < 0.05) ns: non-significant.

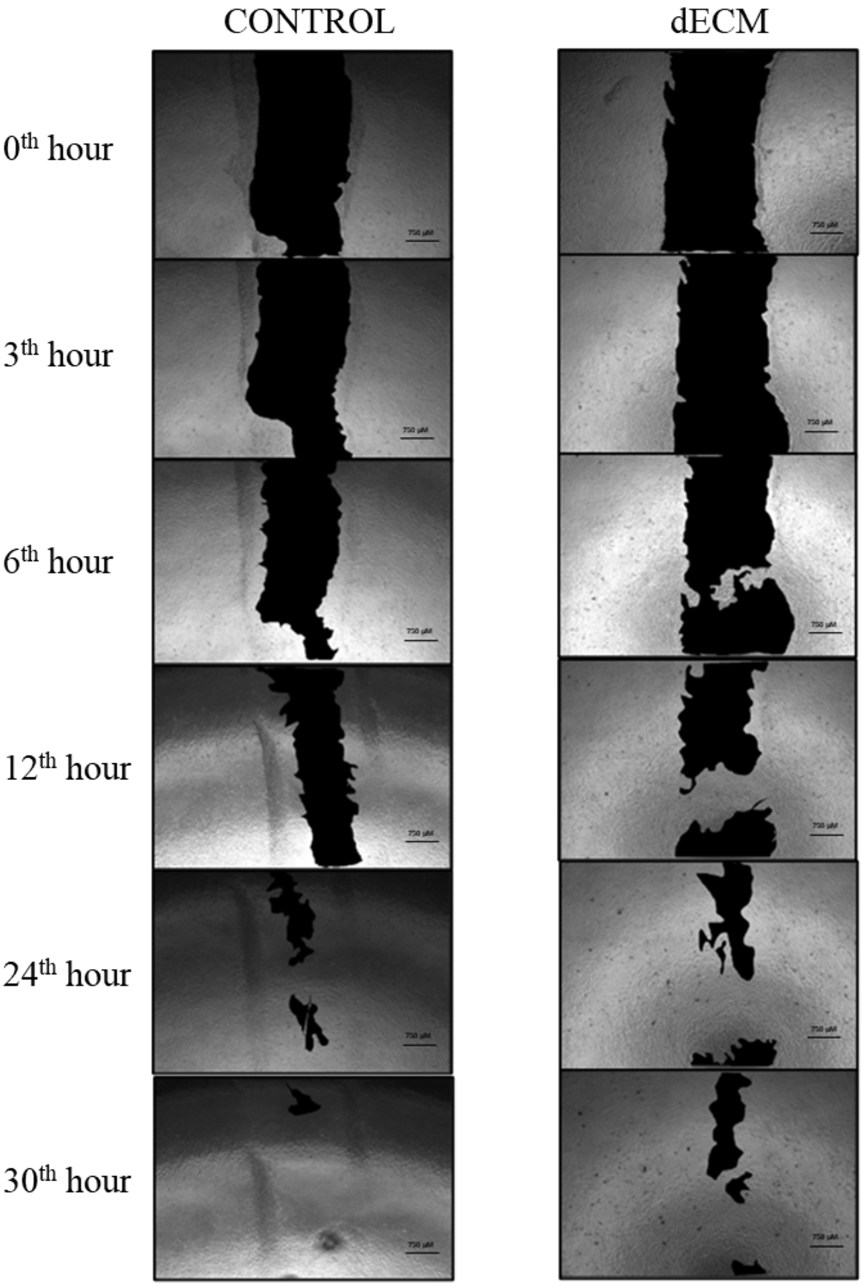

Fig. 11 Scratch assay of ink (GelMA + dECM) on NIH3T3 cells.

3.10 Cytotoxicity analysis of solubilized dECM and GelMA on HepG2 cells

The cytotoxicity of the ink was analysed by MTT assay on two different cell HepG2 and NIH3T3, to understand the effect of the ink on the viability of the cells. Both the cell lines showed good viability when compared to the control. It was found that the HepG2 cells had viability of 90% (Fig. 10A) and NIH3T3 cells had viability of 93.8% (Fig. 10B). The Fig. 10 represents the MTT graph of both the cells which proves that the ink is compatible with cells. Similarly, to confirm the cell viability of the cells exposed to the ink, scratch assay was performed on the NIH3T3 cells (Fig. 11). After 30th hour the scratch in both the control and the test, the scratch was covered by the cells, confirming normal functioning of cells.

3.11 Characterization of 3D bioprinted constructs

3.11.1 Degradation study. Degradation graph demonstrates 3D printed scaffold composition exposed to PBS and culture media (Fig. 12) play critical roles in determining degradation kinetics, which are essential parameters for scaffold design in regenerative medicine and tissue engineering applications. Both groups show increased degradation over time, but scaffolds when subjected to culture media degrade faster than in PBS, at day 21, scaffolds in media reach a degradation rate of about ∼23%, and in PBS ∼16%. The enhanced degradation in media may be due to additional biological and enzymatic components (serum proteins) that are absent in PBS, facilitating faster breakdown of scaffold material.

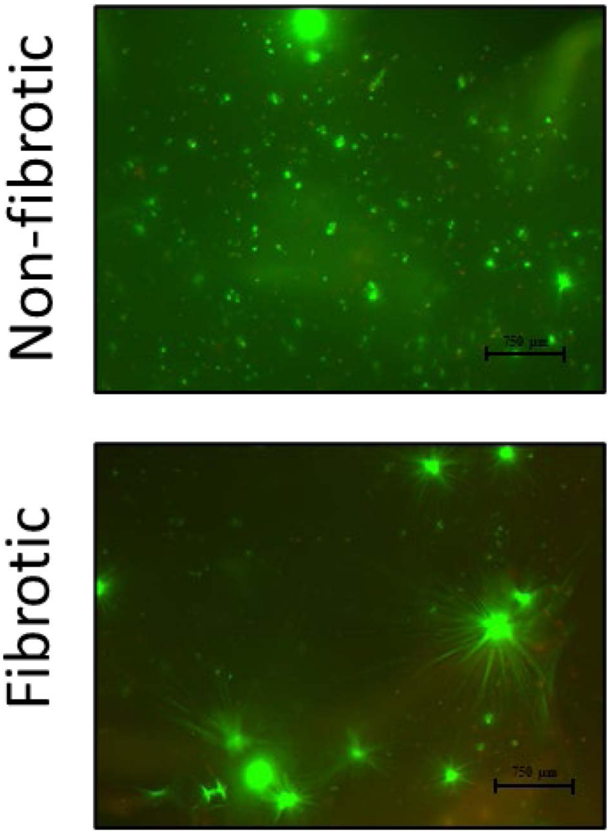

Fig. 13 Live/dead assay of 3D bioprinted non-fibrotic and fibrotic constructs (10× magnification).

3.11.2 Induction of fibrosis. Fibrotic conditions were induced in HepG2 cells cultured on bioprinted constructs by exposure to 10 mM methotrexate, optimized from previous studies, over a 72-hour period. Post-treatment, cell viability was analysed by MTT assay, and morphological evidence of fibrosis was evaluated using H&E staining. Cells were fixed in formaldehyde, sequentially dehydrated using graded ethanol washes,

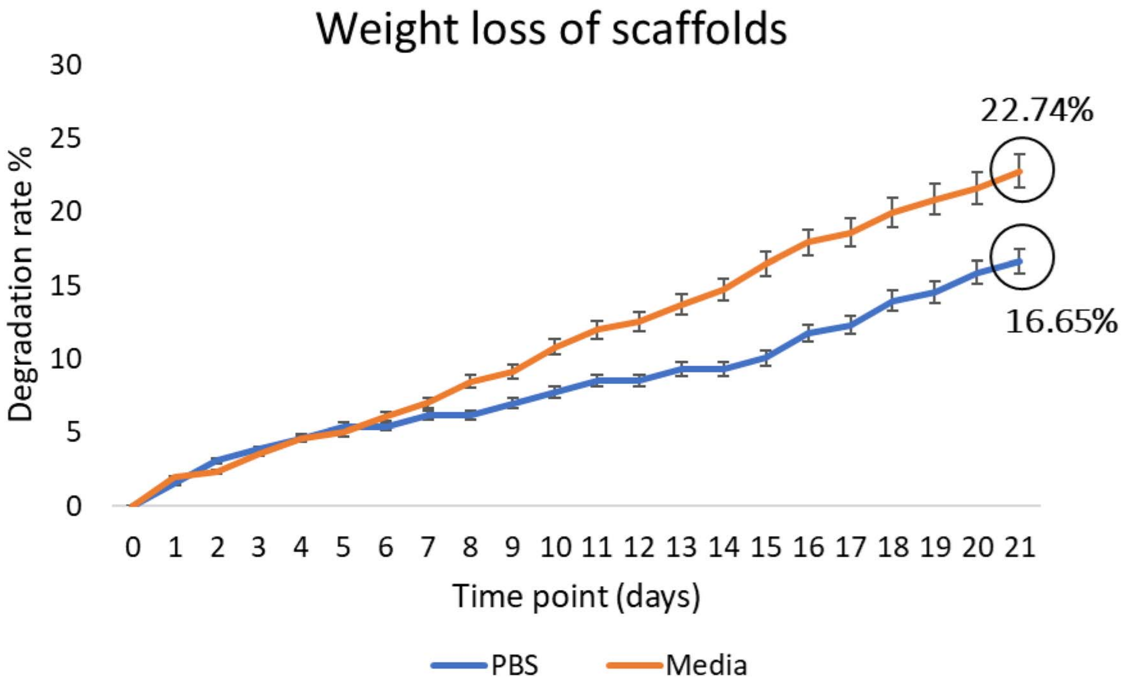

Fig. 12 Degradation rate of scaffolds for 3 weeks in PBS and cell culture medium.

stained, and mounted with DPX prior to microscopic examination.

3.11.3 Live/dead viability assay. A live/dead viability assay was conducted on 3D bioprinted fibrotic scaffolds at Day 3. Scaffolds incubated with MTX exhibited an increased proportion of dead cells, as visualized by Z-stack merged fluorescence images. In contrast, untreated scaffolds demonstrated a predominance of viable cells relative to dead cells, whereas MTX-treated scaffolds exhibited the opposite trend, with a higher number of dead cells observed (Fig. 13). The increased cell death in the fibrotic scaffolds following MTX treatment confirms the cytotoxic effect of the drug within the 3D bioprinted model.

3.11.4 Histological analysis of 3D bioprinted constructs. The H&E-stained images (Fig. 14B) demonstrate the structural transition of bioprinted liver scaffolds upon fibrotic stimulation with MTX, confirming successful fibrosis induction *in vitro*. The switch from round to spindle-shaped cells indicates hepatic stellate cells (HSC) activation, a hallmark of liver fibrosis. Moreover, the increased eosin staining and altered morphology correlate with early fibrotic remodelling. The cells in non-fibrotic sections appear round-shaped, dispersed, and maintain a typical hepatic morphology with no visible architectural distortion or non-myofibroblast-like and Ishak score being 0, indicating no fibrosis (Fig. 14A). The cells in fibrotic sections appear spindle-shaped morphology, contractile morphology, a hallmark of myofibroblast transdifferentiating and contractile morphology indicating activation of HSCs with no visible architectural distortion or non-myofibroblast-like and Ishak score being 3 along with dense eosinophilic regions, suggesting ECM accumulation, one of the classic features of fibrosis (Fig. 14B). Ishak scoring assess the severity and progression of liver fibrosis in clinical and research settings (Fig. 14C) comprises of table describing the Ishak Staging System for liver fibrosis which is used in histopathology to grade the extent of fibrosis in liver biopsy samples. The table has two columns: Ishak score that lists stages from 0 to 6 and histological features describes the specific histological findings in the liver for each stage.[43–45]

3.11.5 Functional analysis of 3D bioprinted constructs. Functional evaluation of 3D bioprinted constructs under non-fibrotic (non-treated) and fibrotic (treated) conditions was

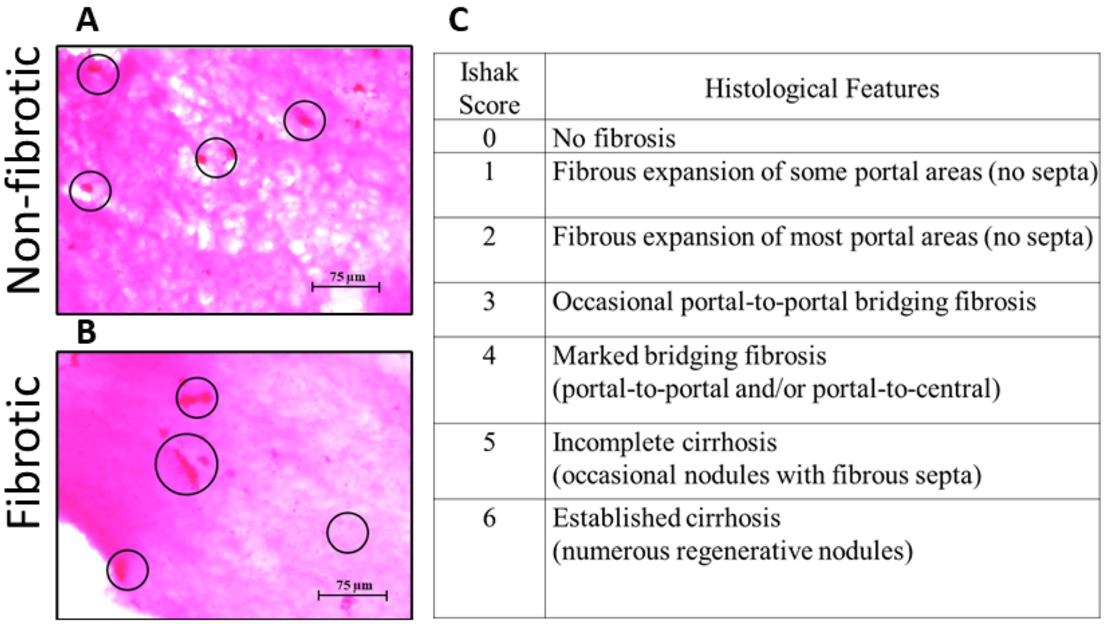

Ishak Score	Histological Features
0	No fibrosis
1	Fibrous expansion of some portal areas (no septa)
2	Fibrous expansion of most portal areas (no septa)
3	Occasional portal-to-portal bridging fibrosis
4	Marked bridging fibrosis (portal-to-portal and/or portal-to-central)
5	Incomplete cirrhosis (occasional nodules with fibrous septa)
6	Established cirrhosis (numerous regenerative nodules)

Fig. 14 H&E staining of 3D bioprinted (A) non-fibrotic and (B) fibrotic scaffolds (40× magnification), (C) Ishak scoring.[37]

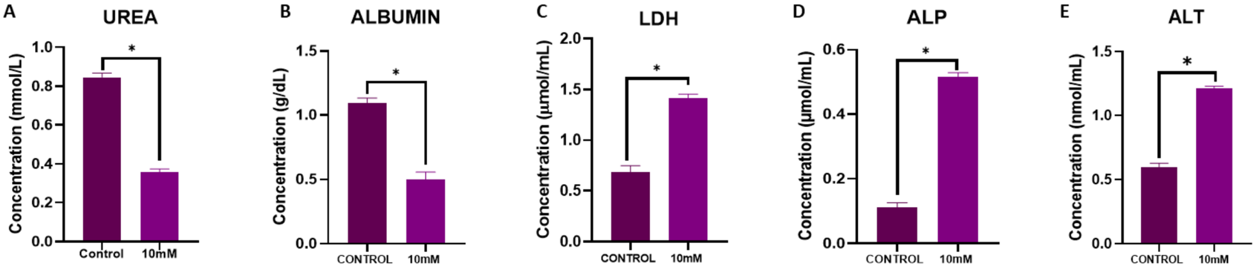

Fig. 15 Functional tests on non-fibrotic and fibrotic constructs; (A) – urea, (B) – albumin, (C) – LDH, (D) – ALP, and (E) – ALT, *: statistically significant ($p < 0.05$).

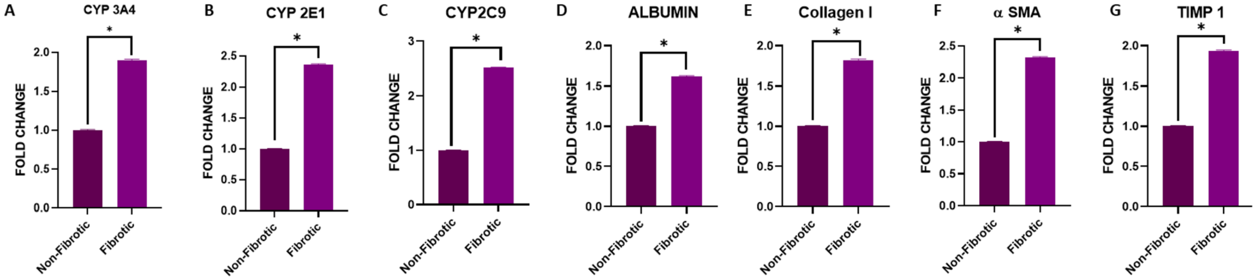

Fig. 16 Gene expression on non-fibrotic and fibrotic constructs; (A) – CYP2A4 (B) – CYP2E1, (C) – CYP 2C9, (D) – albumin, (E) – collagen I, (F) – aSMA and (G) – TIMP 1, *: statistically significant ($p < 0.05$).

performed by quantifying the release of liver-specific biochemical markers (Fig. 15). Non-fibrotic constructs exhibited significantly higher concentrations of albumin, urea, and LDH compared to fibrotic constructs. Conversely, ALP and ALT were significantly elevated in fibrotic constructs compared to controls. These findings suggest altered hepatic functionality consistent with induced fibrotic pathology, confirming the scaffold's responsiveness to biochemical changes associated with liver fibrosis.

3.11.6 Gene expression analysis. Quantitative real-time PCR was conducted to assess gene expression profiles in non-fibrotic and fibrotic 3D bioprinted constructs. Gene expression levels were normalized against the housekeeping gene GAPDH and presented as relative fold changes (Fig. 16). Expression levels of hepatic markers (cytochrome 3A4, cytochrome 2E1, cytochrome 2C9 and albumin) and fibrosis-associated marker (collagen I, alpha-smooth muscle actin and tissue inhibitor of matrix metalloproteinase 1) were significantly upregulated in fibrotic constructs compared to non-fibrotic controls. Elevated expression of these genes in the treated constructs is indicative of successful induction and manifestation of hepatic fibrosis at the molecular level, thus validating the utility of this bioprinted model for studying fibrotic mechanisms.

4 Conclusion

This study demonstrates a robust methodology for the decellularization of rat liver tissues, GelMA synthesis, and development of a biocompatible integrated GelMA–dECM bioink for 3D bioprinting in hepatic tissue engineering. This synergy allows us to achieve both structural fidelity and a more physiologically relevant microenvironment. The decellularization process efficiently preserved essential ECM proteins, GAGs, and scaffold integrity, while GelMA provided the structural stability necessary for scaffold formation and sustained cellular viability and proliferation. Functional and molecular validations confirmed that the 3D bioprinted constructs effectively mimic non fibrotic and methotrexate-induced fibrotic liver conditions. This model provides a better physiological and functional complexity as current 2D and simple 3D cultures often fail to sustain hepatocyte-specific functions over time. Other existing *in vitro* fibrosis models do not capture hallmark fibrogenic responses, this current model demonstrates fibrosis-related markers. This innovative model holds substantial translational promise, specifically as a powerful platform for high-throughput drug screening, toxicity assessment, and precision modeling of liver fibrosis, thereby potentially accelerating therapeutic advancements and translational applicability in hepatic diseases.

Author contributions

Kirthanashri S. V.: conceptualization, investigation, data curation, writing – original draft, editing, reviewing and validation; Mrunmayi Gadre: investigation, data curation, visualization, writing – original draft.

Conflicts of interest

The authors declare no competing interests.

Data availability

The datasets generated and/or analyzed during the current study are available online as the Indian patent, repository (Indian Patent No. 202341045531).

Acknowledgements

The authors would like to thank the Manipal Centre for Biotherapeutic Research, and Manipal Academy of Higher Education, Manipal for the provision of research instruments and infrastructure support.

References

1 R. D. Antarianto, A. A. Prima Dewi, A. Pragiwaksana and J. A. Pawitan, Decellularization of liver cubes using multiple site syringe injection for generating native liver scaffold: Preliminary report, *AIP Conf. Proc.*, 2019, **2193**(1), 040005.

2 L. Alaby Pinheiro Faccioli, G. Suhett Dias, V. Hoff, M. Lemos Dias, C. Ferreira Pimentel, C. Hochman-Mendez, *et al.*, Optimizing the Decellularized Porcine Liver Scaffold Protocol, *Cells Tissues Organs*, 2020, **211**(4), 385–394.

3 J. H. Ghim, K. H. Hussein, K. M. Park and H. M. Woo, Hepatic cell encapsulation using a decellularized liver scaffold, *Biomed. Eng. Lett.*, 2015, **5**(1), 58–64.

4 V. Keriquel, F. Guillemot, I. Arnault, B. Guillotin, S. Miraux, J. Amédée, J. C. Fricain and S. Catros, In vivo bioprinting for computer-and robotic-assisted medical intervention: preliminary study in mice, *Biofabrication*, 2010, **2**(1), 014101.

5 K. Arai, S. Iwanaga, H. Toda, C. Genci, Y. Nishiyama and M. Nakamura, Three-dimensional inkjet biofabrication based on designed images, *Biofabrication*, 2011, **3**(3), 034113.

6 T. Zhang, K. C. Yan, L. Ouyang and W. Sun, Mechanical characterization of bioprinted in vitro soft tissue models, *Biofabrication*, 2013, **5**(4), 045010.

7 A. Kislitsyn, R. Savinkov, M. Novkovic, L. Onder and G. Bocharov, Computational approach to 3D modeling of the lymph node geometry, *Computation*, 2015, **3**(2), 222–234.

8 M. J. Rodriguez, J. Brown, J. Giordano, S. J. Lin, F. G. Omenetto and D. L. Kaplan, Silk based bioinks for soft tissue reconstruction using 3-dimensional (3D) printing with in vitro and in vivo assessments, *Biomaterials*, 2017, **117**, 105–115.

9 S. Tripathi, M. Dash, R. Chakraborty, H. J. Lukman, P. Kumar, S. Hassan, H. Mehboob, H. Singh and H. S. Nanda, Engineering considerations in the design of tissue specific bioink for 3D bioprinting applications, *Biomater. Sci.*, 2025, **13**(1), 93–129.

10 P. S. Gungor-Ozkerim, I. Inci, Y. S. Zhang, A. Khademhosseini and M. R. Dokmeci, Bioinks for 3D bioprinting: an overview, *Biomater. Sci.*, 2018, **6**(5), 915–946.

11 M. Gadre, D. Mallya, M. Kasturi and K. S. Vasanthan, Polymers and Composites in 3D Bioprinting for Regenerative Medicine, *Biomedical Materials and Biofabrication for Regenerative Medicine*, 2024, vol. 26, p. 22.

12 M. Hospodiuk, M. Dey, D. Sosnoski and I. T. Ozbolat, The bioink: A comprehensive review on bioprintable materials, *Biotechnol. Adv.*, 2017, **35**(2), 217–239.

13 H. W. Kang, S. J. Lee, I. K. Ko, C. Kengla, J. J. Yoo and A. Atala, A 3D bioprinting system to produce human-scale tissue constructs with structural integrity, *Nat. Biotechnol.*, 2020, **34**(3), 312–319.

14 S. Bupphathong, C. Quiroz, W. Huang, P. F. Chung, H. Y. Tao and C. H. Lin, Gelatin methacrylate hydrogel for tissue engineering applications—a review on material modifications, *Pharmaceuticals*, 2022, **15**(2), 171.

15 S. Ma, T. Li, Y. Zhu, C. Sun, Z. Liu and H. Zhang, Research progress of gelatin-based biodegradable films, *Sci. Technol. Food Ind.*, 2021, **42**(12), 373–380, DOI: **10.13386/j.issn1002-0306.2020060256**.

16 S. Zhao, Z. Li, B. Sun, W. Zhang and Y. Sun, Gelatin-based materials: fabrication, properties and applications in the food packaging system, *RSC Adv.*, 2025, **15**, 15119–15132, DOI: **10.1039/D5RA03325J**.

17 M. Gadre, M. Kasturi, P. Agarwal and K. S. Vasanthan, Decellularization and their significance for tissue regeneration in the era of 3D bioprinting, *ACS Omega*, 2024, **9**(7), 7375–7392.

18 M. W. McCrary, N. E. Vaughn, N. Hlavac, Y. H. Song, R. A. Wachs and C. E. Schmidt, Novel sodium deoxycholate-based chemical decellularization method for peripheral nerve, *Tissue Eng., Part C*, 2020, **26**(1), 23–36.

19 D. Boso, E. Carraro, E. Maghin, S. Todros, A. Dedja, M. Giomo, N. Elvassore, P. De Coppi, P. G. Pavan and M. Piccoli, Porcine decellularized diaphragm hydrogel: a new option for skeletal muscle malformations, *Biomedicines*, 2021, **9**(7), 709.

20 H. Liu, Y. Gong, K. Zhang, S. Ke, Y. Wang, J. Wang and H. Wang, Recent advances in decellularized matrix-derived materials for bioink and 3D bioprinting, *Gels*, 2023, **9**(3), 195.

21 R. O. Moore, J. L. Madara and R. J. MacLeod, Enterocytes adhere preferentially to collagen IV in a differentially regulated divalent cation-dependent manner, *Am. J. Physiol.: Gastrointest. Liver Physiol.*, 1994, **266**(6), G1099–G1107.

22 M. Caralt, J. S. Uzarski, S. Iacob, K. P. Obergfell, N. Berg, B. M. Bijonowski, K. M. Kiefer, H. H. Ward, A. Wandinger-Ness, W. M. Miller and Z. J. Zhang, Optimization and critical evaluation of decellularization strategies to develop renal extracellular matrix scaffolds as biological templates for organ engineering and transplantation, *Am. J. Transplant.*, 2015, **15**(1), 64–75.

23 J. Cheng, C. Wang and Y. Gu, Combination of freeze-thaw with detergents: a promising approach to the decellularization of porcine carotid arteries, *Bio-Med. Mater. Eng.*, 2019, **30**(2), 191–205.

24 K. Y. Chi, G. Kim, J. S. Son, J. Han and J. H. Kim, Recent Advances in Three-Dimensional In Vitro Models for Studies of Liver Fibrosis, *Tissue Eng. Regener. Med.*, 2025, **13**, 1–7.

25 N. Roehlen, E. Crouchet and T. F. Baumert, Liver fibrosis: mechanistic concepts and therapeutic perspectives, *Cells*, 2020, **9**(4), 875.

26 E. Moradi, S. Jalili-Firoozinezhad and M. Solati-Hashjin, Microfluidic organ-on-a-chip models of human liver tissue, *Acta Biomater.*, 2020, **116**, 67–83.

27 K. Yue, G. Trujillo-de Santiago, M. M. Alvarez, A. Tamayol, N. Annabi and A. Khademhosseini, Synthesis, properties, and biomedical applications of gelatin methacryloyl (GelMA) hydrogels, *Biomaterials*, 2015, **73**, 254–271.

28 J. S. Lee, J. Shin, H. M. Park, Y. G. Kim, B. G. Kim, J. W. Oh and S. W. Cho, Liver extracellular matrix providing dual functions of two-dimensional substrate coating and three-dimensional injectable hydrogel platform for liver tissue engineering, *Biomacromolecules*, 2014, **15**(1), 206–218.

29 G. Mazza, W. Al-Akkad and K. Rombouts, Engineering in vitro models of hepatofibrogenesis, *Adv. Drug Delivery Rev.*, 2017, **121**, 147–157.

30 H. Yang, L. Sun, Y. Pang, D. Hu, H. Xu, S. Mao, W. Peng, Y. Wang, Y. Xu, Y. C. Zheng and S. Du, Three-dimensional bioprinted hepatorganoids prolong survival of mice with liver failure, *Gut*, 2021, **70**(3), 567–574.

31 J. Wang, M. Sun, W. Liu, Y. Li and M. Li, Stem cell-based therapies for liver diseases: an overview and update, *Tissue Eng. Regener. Med.*, 2019, **16**(2), 107–118.

32 D. G. Nguyen, J. Funk, J. B. Robbins, C. Crogan-Grundy, S. C. Presnell, T. Singer and A. B. Roth, Bioprinted 3D primary liver tissues allow assessment of organ-level response to clinical drug induced toxicity in vitro, *PLoS One*, 2016, **11**(7), e0158674.

33 L. M. Norona, D. G. Nguyen, D. A. Gerber, S. C. Presnell, M. Mosedale and P. B. Watkins, Bioprinted liver provides early insight into the role of Kupffer cells in TGF-β1 and methotrexate-induced fibrogenesis, *PLoS One*, 2019, **14**(1), e0208958.

34 X. Ma, X. Qu, W. Zhu, Y. S. Li, S. Yuan, H. Zhang, J. Liu, P. Wang, C. S. Lai, F. Zanella and G. S. Feng, Deterministically patterned biomimetic human iPSC-derived hepatic model via rapid 3D bioprinting, *Proc. Natl. Acad. Sci. U. S. A.*, 2016, **113**(8), 2206–2211.

35 M. Kasturi and K. S. Vasanthan, Harvesting decellularized liver extracellular matrix from rodents for 3D scaffold fabrication, *Artif. Cells Nanomed. Biotechnol.*, 2024, **52**(1), 175–185.

36 L. Alaby Pinheiro Faccioli, G. Suhett Dias, V. Hoff, M. Lemos Dias, C. Ferreira Pimentel, C. Hochman-Mendez, *et al.*, Optimizing the Decellularized Porcine Liver Scaffold Protocol, *Cells Tissues Organs*, 2020, **211**(4), 385–394.

37 J. H. Ghim, K. H. Hussein, K. M. Park and H. M. Woo, Hepatic cell encapsulation using a decellularized liver scaffold, *Biomed. Eng. Lett.*, 2015, **5**(1), 58–64.

38 M. Vidhi, S. V. Kirthanashri, S. Varadharajan and N. S. Raviraja, Process For Formulation Of A Ink For Printing 3D Tubular Structures, *Indian Pat.*, 202341045531, 2023.

39 C. Pakhomova, D. Popov, E. Maltsev, I. Akhatov and A. Pasko, Software for bioprinting, *Int. J. Bioprint.*, 2020, **6**(3), 279.

40 T. M. Bücking, E. R. Hill, J. L. Robertson, E. Maneas, A. A. Plumb and D. I. Nikitichev, From medical imaging data to 3D printed anatomical models, *PLoS One*, 2017, **12**(5), e0178540.

41 K. A. Abdullah and W. Reed, 3D printing in medical imaging and healthcare services, *J. Med. Radiat. Sci.*, 2018, **65**(3), 237–239.

42 P. P. Borthakur, A. Das, J. J. Sahariah, P. Pramanik, E. Baruah and K. Pathak, Revolutionizing Patient Care: 3D Printing for Customized Medical Devices and Therapeutics, *Biomed. Mater. Devices*, 2025, 1–28.

43 M. Shabanian, Z. Taylor, C. Woods, A. Bernieh, J. Dillman, L. He, S. Ranganathan, J. Picarsic and E. Somasundaram, Liver fibrosis classification on trichrome histology slides using weakly supervised learning in children and young adults, *J. Pathol. Inf.*, 2025, **16**, 100416.

44 C. Ercan, K. Kordy, A. Knuuttila, X. Zhou, D. Kumar, V. Koponen, P. Mesenbrink, S. Eppenberger-Castori, P. Amini, M. C. Pedrosa and L. M. Terracciano, A deep-learning-based model for assessment of autoimmune hepatitis from histology: AI (H), *Virchows Arch.*, 2024, **485**(6), 1095–1105.

45 A. Watson, L. Petitjean, M. Petitjean and M. Pavlides, Liver fibrosis phenotyping and severity scoring by quantitative image analysis of biopsy slides, *Liver Int.*, 2024, **44**(2), 399–410.